Contents lists available at ScienceDirect

Earth and Planetary Science Letters

The slow slip event cycle along the Izmit segment of the North Anatolian Fault

Estelle Neyrinck [a,*], Baptiste Rousset [a], Cécile Doubre [a], Luis Rivera [a], Cécile Lasserre [b],
Marie-Pierre Doin [c], Philippe Durand [d], Roger Bilham [e], Ziyadin Çakir [f],
FLATSIM Working Group

[a] *Institut Terre et Environnement de Strasbourg UMR7063, Université de Strasbourg/CNRS/ENGESS, 5 Rue René Descartes, Strasbourg, 67000, France*
[b] *Université Lyon 1, ENSL, CNRS, LGL-TPE, Lyon, 69000, France*
[c] *University Grenoble Alpes, University Savoie Mont Blanc, University Gustave Eiffel, CNRS, IRD, ISTerre, Grenoble, 69000, France*
[d] *CNES, Toulouse, 31000, France*
[e] *University of Colorado, Boulder, CO 80309, United States*
[f] *Istanbul Technical University, Istanbul, Türkiye*

ARTICLE INFO

ABSTRACT

The occurrence of aseismic creep along seismogenic faults significantly impacts seismic hazard assessment by releasing accumulated stress and reducing the slip deficit. Since the 1999 M_w7.6 Izmit earthquake on the North Anatolian Fault in Türkiye, while aseismic creep has been observed as a postseismic response to the Izmit rupture, additional slow slip events were detected in 2015 and 2016, accommodating several millimeters of relative displacement over periods of approximately one month. By automating Interferometry Synthetic Aperture Radar time series processing from 2016 to 2021 (FLATSIM project) and applying specific post-processing, we extract the tectonic signal to estimate the slip dynamics of the Izmit segment, including the detection and characterization of slow slip events. Modeling the slip distribution at depth on a 2D fault interface within a layered elastic half-space, we estimate a locking depth of 11 km and steady creep between 2 and 5 km. Above the steady creep zone, we identify two new shallow slow slip events in March 2018 and November 2019, with moment magnitudes of 4.3 and 4.4, respectively. Based on creepmeter measurements, we estimate a lateral propagation velocity of 6.4 km/day for the 2019 event. The location of these shallow slow slip events above the sedimentary-bedrock interface suggests a critical role of variations in frictional properties in the occurrence of transient slip events.

1. Introduction

The growing number of seismological and geodetic observations has enabled to refine the seismic and aseismic slip behaviors of worldwide active faults (e.g. Bürgmann, 2018). A large diversity of aseismic behaviors is observed, ranging from steady-state creep to slow slip events (SSEs), also referred to as transient creep events, that can last from minutes to years. The first observations of aseismic creep came from Steinbrugge et al. (1960) who highlighted the existence of shallow creep on a continental strike-slip fault by analyzing distortions on constructions in the cities above San Andreas Fault (SAF) zone. Since these observations, aseismic deformation on faults has been extensively studied using various geodetic techniques including Global Navigation Satellite System (GNSS), strainmeters, creepmeters and Interferometry Synthetic Aperture Radar (InSAR). Transient SSEs have mostly been detected on subduction zones including the Cascadia subduction zone (Dragert et al., 2001), the Nankai subduction zone (Obara et al., 2004), in Mexico (Radiguet et al., 2011), New Zealand (Wallace et al., 2016), Alaska (Rousset et al., 2019), Costa Rica (Jiang et al., 2012), Ecuador (Vaca et al., 2018), and more recently in Chile (Klein et al., 2017). They have been observed at both the deep (e.g. Dragert et al., 2001; Obara et al., 2004) and shallow (McCaffrey et al., 2008; LaBonte et al., 2009, e.g.) ends of the seismogenic zone. Several continental strike-slip faults appear to also be affected by SSEs such as the SAF (e.g. Rousset et al., 2019; Gittins and Hawthorne, 2022), the San Jacinto Fault close to the Anza gap (Inbal et al., 2017), the Superstition Hills Fault (Wei et al., 2009), the Haiyuan Fault (Jolivet et al., 2012) and the North Anatolian Fault (NAF) (Rousset et al., 2016; Aslan et al., 2019; Jolivet et al., 2023).

On continental strike-slip faults, SSEs predominantly occur within the upper few kilometers, exhibiting slip amplitudes ranging from millimeters to centimeters and equivalent moment magnitudes from 4 to 5 where estimable (e.g. Wei et al., 2009; Rousset et al., 2016; Materna et al., 2024). These events recur every few months to years or decades (Wei et al., 2013; Bilham et al., 2016; Vavra et al., 2024) and recurrence intervals can transition from shorter to longer periods during the postseismic phase (Wei et al., 2013). The SSEs timing can also be influenced by dynamic stresses from nearby large earthquakes (Wei et al., 2011).

The primary explanation for shallow creep on strike-slip faults is the presence of poorly consolidated sediments close to the surface (Scholz, 1998). Lateral alternations of creeping and locked segments could be due to lateral variations in mineralogical composition of the gouge, with talc and serpentine for example, deforming and transforming into low-friction minerals, favoring creep (e.g. Bürgmann, 2018; Kaduri et al., 2017). The presence of high pore fluid pressure on some segments may also enhance aseismic slip, as evidenced in geothermal contexts (e.g. Guglielmi et al., 2015). In the framework of rate-and-state friction seismic cycle models for purely elastic media, shallow creep can be reproduced with a shallow velocity-strengthening layer (Kaneko et al., 2013). The emergence of transient SSEs can arise by adding a layer of velocity-neutral friction also referred to as conditionally stable (Wei et al., 2013). However, the small number of SSE observations on strike-slip fault contexts limits our understanding of the underlying physical processes and key mechanical parameters. A better description of the mechanisms governing the various aseismic slip behaviors on faults and the possible interactions between seismic and aseismic slips throughout the various phases of the seismic cycle is crucial to improve seismic hazard models (Avouac, 2015).

In this paper, we focus on the Izmit segment of the NAF in Türkiye where aseismic creep is observed since the 1999 $M_w7.6$ Izmit earthquake from geodetic measurements (Cakir et al., 2012; Hussain et al., 2016; Aslan et al., 2019; Özarpacı et al., 2020). Based on automatically processed Sentinel-1 InSAR time series from 2016 to 2021, we apply a sequence of post-processing steps to extract the tectonic signal and study the slip behavior of the segment, in comparison with creepmeter records with higher temporal resolution.

2. Tectonic context

The right-lateral strike-slip NAF located between the Anatolia and Eurasia plates, with a relative velocity of $24 \pm 1 \; mm/yr$ (McClusky et al., 2000; Reilinger et al., 2006; Nocquet, 2012), crosses Türkiye from East to West over a length of $1600 \; km$. Since the 1930's, it has been affected by a seismic sequence that includes $7 \; M_w \geq 7$ earthquakes, propagating westwards from Erzincan to the Izmit segment (Fig. 1), until the offshore segment below the Marmara Sea which remains a seismic gap and threatens the region of the megalopolis of Istanbul (Stein et al., 1997).

The two last $M_w7.6$ and $M_w7.2$ earthquakes of this sequence ruptured in 1999 the Izmit and Düzce segments (red line Fig. 1B), respectively. The coseismic deformation of the Izmit mainshock has been widely studied, using seismic data (e.g. Bouchon et al., 2001), geodetic data including SAR acquisitions and GNSS data (e.g. Delouis et al., 2002; Feigl et al., 2002) and field observations (e.g. Barka, 2002). The Izmit bilateral rupture from the epicenter (40.76°N, 29.97°E) led to numerous coseismic slip models showing between two and three main slip asperities, with a slip amplitude reaching $8 \; m$ (e.g. Delouis et al., 2002; Feigl et al., 2002). The $M_w \geq 3$ aftershocks are concentrated on the rupture segment, leading to the nucleation of the Düzce earthquake 87 $days$ later and a seismic quiescence on the Izmit segment after the Düzce rupture (Karabulut et al., 2011).

Studies of several time periods following the mainshock reveal a postseismic phase in two stages: i) rapid deep afterslip in areas surrounding the coseismic slip during the first ~ 2.5 $years$ (e.g. Bürgmann et al., 2002; Hearn et al., 2002), ii) viscoelastic relaxation of the lower crust

and upper mantle over the decades following the earthquake (Ergintav et al., 2009), as shown by Hearn et al. (2009) and Wang et al. (2009) who used various rheological models to compute the postseismic deformation and found a viscosity for the lower crust and the upper mantle of $\sim 2.10^{18} - 5.10^{19} \; Pa.s$ and $\sim 7.10^{19} - 2.10^{20} \; Pa.s$, respectively. Comparison of afterslip models indicates a common slip area that rapidly initiated below the Izmit segment at a depth of $12 - 24 \; km$ with a maximum amplitude of $2 \; m$ (Çakir et al., 2003).

In addition to the deep afterslip and the viscoelastic deformation, the shallow part of the Izmit segment is slipping aseismically since the mainshock, raising the question whether this on-going segment behavior is related to the postseismic phase or is more perennial and corresponds to the interseismic deformation. Cakir et al. (2012) showed that the Izmit segment started to creep after the 1999 earthquake on the first kilometers of the sub-surface down to depths of $4 - 5 \; km$ with a creeping rate of up to 10 mm/yr computed over the 2003-2009 period. It showed that some portions of this segment can slip both seismically and aseismically. By using InSAR, GNSS, and creepmeters data, the aseismic creep along the Izmit segment has been confirmed until 2017 (Cakir et al., 2012; Hussain et al., 2016; Aslan et al., 2019; Özarpacı et al., 2020), with a locking depth estimated between 10 and 18 km and shallow steady creep of from 5 to 10 mm/yr, located between the surface and 8 km depth, depending on studies. Recently, Aslan et al. (2019) highlighted a 1 $month$-long SSE in December 2016 causing a surface relative displacement of 10 mm, by using Sentinel-1 InSAR time series and creepmeter data collected close to Izmit (Fig. 1C). Özarpacı et al. (2020) detected another transient event, also recorded by the Izmit creepmeter in September 2015, as well as with campaign GNSS measurements acquired close to the fault.

3. InSAR analysis

3.1. Interferograms and time series processing

By exploiting Sentinel-1 A and B SAR acquisitions, which benefit from repeat acquisition times of 6 days, we aim to characterize the deformation on the Izmit segment with a high temporal resolution from 2016 to 2021, i.e. extending the time period with respect to previous studies. The interferograms and InSAR time series used in this work have been processed in the framework of the FLATSIM *ForM@Ter LArge-Scale Multi-Temporal Sentinel-1 InterferoMetry Service* project, operated by the French *Centre National d'Études Spatiales* (CNES) (Thollard et al., 2021). The processing workflow follows the New Small Baseline (NSBAS) approach (Doin et al., 2011): a selection of bursts, image co-registration and correlation, evaluation of the spectral diversity (Grandin, 2015), range estimate relative to the Digital Elevation Model (DEM) and precise orbit corrections. Interferogram networks are built by minimizing the perpendicular and temporal baselines (up to one year to reduce the impact of phase biases). Atmospheric contributions are addressed for each interferogram, based on global atmospheric models, using the ERA-5 meteorological analysis from the European Centre for Medium-Range Weather Forecasts (ECMWF) (e.g. Jolivet, 2011). Finally, the time series are calculated from the inversion of the interferometric phases.

We use the results from three 250 km-wide tracks covering the Izmit segment of the NAF (Fig. 1B): two ascending ones (A058 and A160), and a descending one (D138). The Fig. S1 in the Supplementary Materials gives the interferogram networks with the number of SAR images and interferograms used for the time series analysis. The common time period covered by the time series of the three tracks is from February 2015 to April 2021. In order to remove the pixels with abnormal noise levels, we kept only the time series corresponding to the pixels with a Root Mean Square (RMS) misclosure lower than 1.5 rad in each interferogram and using at least 900 interferograms per pixel to derive the time series ($63 - 68\%$ of the initial pixels - Fig. S2). The mean InSAR Line Of Sight (LOS) velocities of the three tracks are shown in Fig. 2 - A and B.
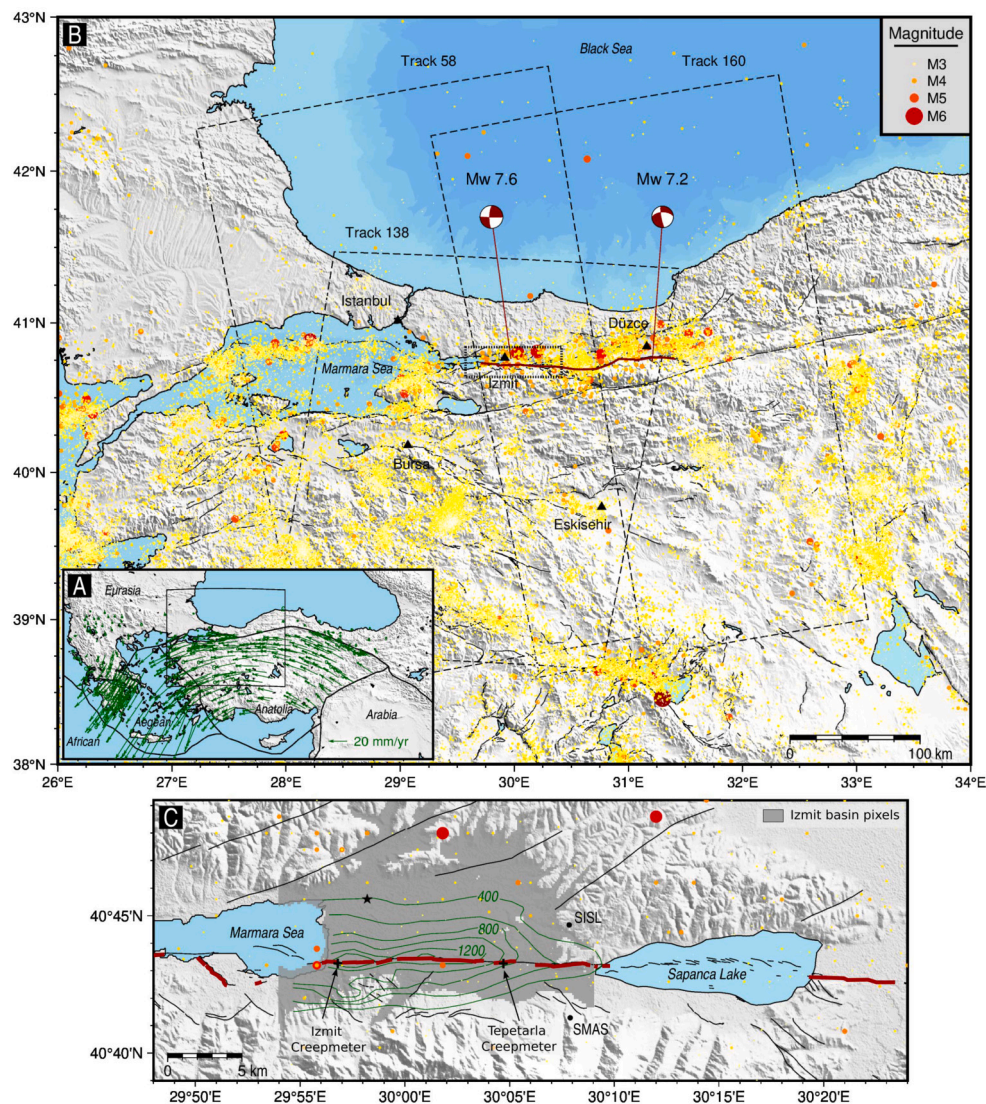
Fig. 1. Tectonic settings and coverage of the InSAR data. (A) GNSS velocity field from England et al. (2016) of the Anatolia and the Aegean plates relative to Eurasia. The horizontal velocities are represented by the green arrows. The tectonic plates are delineated by the bold dark lines. The black rectangle corresponds to the area shown in B. (B) Earthquakes from the AFAD catalog over the 1999-2021 period are shown by colored dots. The focal mechanisms are for the 1999 M_w7.6 Izmit (West) and the 1999 M_w7.2 Düzce (East) earthquakes. The corresponding surface rupture trace is indicated by the bold red line (Barka, 2002). The geological faults are shown by the black lines (Emre et al., 2018). The dashed rectangles correspond to the three InSAR tracks used in this study, and the dotted rectangle corresponds to the cover of the bottom map. (C) Bedrock depth (green lines) within the Izmit basin based on gravity data from Özalaybey et al. (2011). The gray zone shows the pixels within the Izmit basin, with an elevation lower than 150 *m*. The black star corresponds to the 1999 Izmit earthquake epicenter. The two black crosses and the two black dots show the locations of two creepmeters installed along the Izmit segment and of the campaign GNSS stations (SISL, SMAS), respectively. The bold red line corresponds to the surface rupture of the Izmit earthquake from Barka (2002).

3.2. InSAR referencing relative to GNSS velocities

We use the velocity field centered on the studied area relative to the fixed Eurasia plate calculated from survey and continuous GNSS measurements by England et al. (2016) covering the Anatolia plate (Fig. 1A) to reference the InSAR data. The details are explained in the Appendix A.

3.3. Extraction of seasonal signals

Most of the LOS displacement time series across the tracks are affected by strong seasonal signals. To isolate the tectonic signal, we model the seasonal signal for each pixel with annual periodic terms. Details of the method including specific referencing of the seasonal terms are described in the Appendix B.

3.4. Horizontal and vertical decomposition

The mean strike of the Izmit segment being fixed to $N90°$, we combine LOS time series corrected from the seasonal effects and referenced by GNSS velocities from the two ascending and the descending tracks, and convert them into horizontal East-West and vertical displacement time series. We consider that the North-South displacements are negligible. The method is described in the Appendix C. Finally, we obtain four time series: the East-West and the vertical cumulative displacement time series for the two ascending/descending couples of tracks. To describe the pairs of tracks used in each decomposition, we specify the set of data with the following terms *TA058-D138* and *TA160-D138*, corresponding to the numbers of the ascending (A) and descending (D) tracks.

Because the Izmit segment is located in the far range of the track A058 where sensitivity to vertical displacements is lower than in the near range, we focus in the main text on the East-West time series based

on the pair of tracks *TA058-D138*. The results for the second pair *TA160-D138* are shown in the Supplementary Materials.

3.5. Extraction of the tectonic signal

To extract small amplitude deformation within the area of interest (Fig. 2 - C and D) related to slip on the top first kilometers of the Izmit segment interface, we apply additional corrections. We first correct for remaining long-wavelength signals that are non-tectonic, possibly due to orbit errors, tides or atmospheric signals. To do so, (i) we remove a linear temporal trend in each pixel time series, then (ii) we flatten each residual epoch displacement map, and finally (iii) we add back the linear trend. This step enables to reduce the mean standard deviation of the time series from 1.71 *cm* to 1.05 *cm*.

As shown in Fig. 1C, the surface trace of the Izmit segment cuts through a Quaternary basin. Horizontal time series throughout the basin exhibit high-frequency temporal noise. To address this noise, we apply blind source separation using Independent Component Analysis (ICA) (e.g. Maubant et al., 2020). More details on this method are described in the Appendix D. The decomposition is only applied to pixels within the basin selected based on an elevation threshold (≤ 150 *m* - gray area Fig. 1C), on the temporally detrended horizontal time series. By removing two sources extracted by ICA, we reduce the average time series variances within the Izmit basin by 83%. The spatial distribution of the components (Fig. S4 - A and C) corresponds to a ramp within the basin, possibly due to residual low-elevation atmospheric signals.

4. Mean velocities and seasonal signals analysis

4.1. Mean horizontal East-West signal

On the mean East-West velocity map (Fig. 2D), the main signal is the strong gradient located along the NAF, consistent with the interseismic deformation accommodating the right-lateral relative motion of the plates. By comparing the extracted velocities from 80 *km*-long fault perpendicular profiles (red profile on Fig. 2E), we estimated a far field relative motion of 2.26 ± 0.1 *cm/yr* by using far field linear fits, in agreement with previous estimations (McClusky et al., 2000; Reilinger et al., 2006; Nocquet, 2012). Lateral variations of the velocity gradient in the near fault are visible along the NAF, with a stronger gradient across the Izmit segment as shown by the profile Fig. 2E, and a smoother one across the Adapazari segment (eastern part of the study zone - Fig. S7). These lateral variations confirm that shallow creep is occurring along the Izmit segment, while the fault interface of the Adapazari segment is locked from the surface to a greater depth (Aslan et al., 2019).

4.2. Mean vertical signal

On the mean vertical velocity field (Fig. 2C), the Adapazari, Gölcük and Izmit basins are affected by subsidence (from 0.5 to 5 *cm/yr* in the Adapazari basin). On the north of the NAF, many pixels located outside of these Quaternary basins also have a negative mean vertical velocity, mostly correlated with westward motion, inconsistent with the expected tectonic deformation. Possible explanations for this signal could be either short-term phase biases or variations of temporal coherence due to soil moisture or vegetation growth, these pixels being located in vegetated areas (e.g. crops, forests). However, we did not succeed to find a good metrics to mask out these pixels. Because the affected pixels are relatively far from the fault, they do not impact the extraction of the tectonic signal in this study.

Along the Izmit segment, no vertical motion is observed in the vicinity of the fault, except within 3 *km*-wide areas located south of the NAF (zoom on Fig. S8A) and affected by subsidence, likely due to local hydrological effects. The fault-perpendicular profile of the mean vertical velocity (the blue profile on Fig. 2E) reveals no deformation at the location of the fault.

4.3. Seasonal signals

Similar to the linear terms, we transform the two LOS displacement fields corresponding to the seasonal terms *C* and *D* from the equation (B.1) into horizontal East-West and vertical displacement fields by combining the seasonal terms from ascending and descending tracks (Figs. S9 and S10). The profiles perpendicular to the NAF confirm that the slip on the fault is not modulated by the seasonal oscillations on the Izmit basin. More details are given in section 1.3 in the Supplementary Materials.

5. Creep dynamics along the Izmit segment

In this section, we compare the InSAR relative displacements between pixels on both sides of the fault with the data collected at two creepmeters installed on the Izmit segment: the 'Izmit creepmeter' on its western part (40.7211°N-29.9465°E) and the 'Tepetarla creepmeter' on its eastern part (40.7210°N-30.0784°E) (shown in Fig. 1C). The temporal coverage of the creepmeters is from 2015 to 2020, but is discontinuous because of technical issues like flooding.

5.1. Fault relative displacement

5.1.1. Transient creep events

We analyze the East-West displacement time series corrected from non-tectonic signals close to the fault in order to focus on the shallow creep dynamics of the Izmit segment. We compute the mean time series of the pixels located within two 600 *m* by 600 *m* squares, located on each side of the fault and centered 700 *m* from the fault trace. We then compute the difference of both time series to obtain the Izmit along-strike relative displacement. Fig. 3B shows three examples of cumulative relative displacement time series obtained at longitudes *E*029.95°, *E*030.01° and *E*030.08°. All three relative time series exhibit a linear trend corresponding to an average velocity of ~ 5.3 *mm/yr* at the western location, ~ 6.7 *mm/yr* at the middle one and ~ 6.0 *mm/yr* at the eastern one. Superimposed on these positive trends, clear temporal variations are observed in the time series, including transient accelerations in early 2018 and late 2019 at the two eastern locations.

Fig. 3C shows the detrended cumulative relative displacement time series, where the linear trends computed between the acceleration episodes have been removed. It highlights the relative displacement amplitude during the transient accelerations in March 2018 and in November 2019 of up to 10 *mm* of cumulative offsets during the two events. The second transient event coincides in time with a transient observed by both creepmeters (Fig. 3D) with transient amplitudes of 2 *mm* at the Izmit creepmeter and 4 *mm* at the Tepetarla creepmeter.

To constrain the lateral extent of these transient events, we analyze the relative displacement along the entire Izmit segment (Fig. 3A). The two transient events of 2018 and 2019 are clearly visible, extending along ~ 13 *km*, from the Marmara sea to latitude *E*030.10°. Another transient event emerging from the noise is also visible in 2016 but with lower amplitude than the two others. It coincides in time with a 1 *mm* transient recorded by the Izmit creepmeter (Fig. 3D) and has also been documented by Aslan et al. (2019) who estimated an offset of about 10 *mm* of East-West displacement with InSAR measurements.

5.1.2. Analysis of transient and inter-transient periods

To compare the total displacements due to the transient events and the periods between them ('inter-transient' periods), we define two complete cycles composed of one main transient event and one inter-transient period. The first cycle starts on January 20, 2017 and ends on May 20, 2018, including the 2018 transient slip event, while the second cycle starts on May 21, 2018 and ends on January 10, 2020, including the 2019 transient slip event.

Fig. 4 shows the cumulative displacements recorded during each period. The spatial extent of the three transient events is different. The
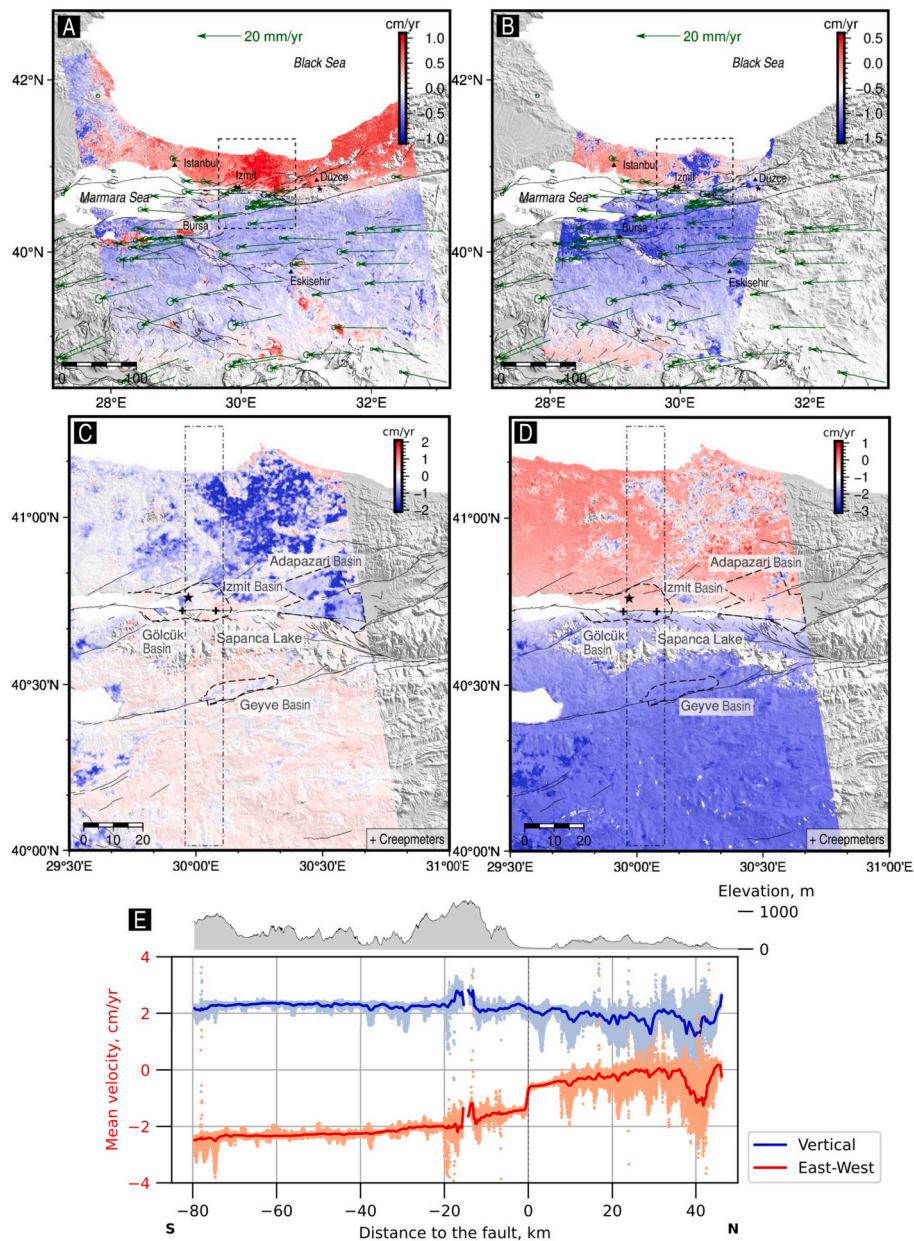
Fig. 2. InSAR LOS, horizontal and vertical velocity fields. (A, B) Maps of the mean LOS velocities of (A) ascending tracks A058 and A160 and (B) descending track D138. Red and blue values correspond to velocities in cm/yr away and towards the satellite, respectively. The fault network is represented by the black lines from Emre et al. (2018). The green arrows correspond to the GNSS velocities in a fixed Eurasia reference frame, obtained from England et al. (2016), and used to reference the East-West InSAR velocity field. The two black stars correspond to the 1999 Izmit $M_w7.6$ and the 1999 Düzce $M_w7.2$ earthquakes epicenters and the main cities are located by black triangles. The dotted rectangle corresponds to the cropped zone used in this study. (C, D) Mean vertical (C) and horizontal East-West (D) velocities after decomposition for tracks A058 and D138, and GNSS referencing. (C) Mean vertical velocities in cm/yr with in red and blue, up and down displacements, respectively. (D) Mean East-West velocities in cm/yr with in red and blue, eastward and westward displacements, respectively. The dotted lines highlight the major Quaternary basins named after the main city within them, Gölcük-Izmit, Adapazari and Geyve. (E) Fault-perpendicular profiles corresponding to the dotted-dashed rectangles on the middle maps of mean vertical (blue) and mean East-West (red) velocities, and the elevation (upper profile in gray). The thick lines correspond to the averaged velocities (smoothed over moving windows of $18\ days$). For graphical reasons, the vertical velocity profile is shifted by $+2\ cm/yr$. The corresponding results obtained with the decomposition *TA160-D138* are shown Fig. S6.

2016 event (panel A) ruptures mostly the western part of the segment over a $\sim 8\ km$-long distance, and both the 2018 and 2019 events (panels B and C, respectively) happen on the central part of the segment over a $\sim 13\ km$-long distance. The shape of the cumulative displacements during these events is mostly symmetrical, with maximum amplitude at the center. This representation highlights a lack of displacement during the transient events on the eastern part of the segment. The analysis of the cumulative relative displacements during the inter-transient periods (panels D and E) shows a cumulative relative displacement of 1 cm on

average everywhere along the segment. Lateral variations are evolving between the two inter-transient periods showing a temporal evolution of either local noise or potential other transient slip events producing a signal close to the noise level.

On Fig. 4F, we sum the relative displacements for the two 2018 and 2019 transient slip events and 2016-2017 and 2017-2018 inter-transient periods. Despite the variations of cumulative relative displacement during the inter-transient periods, the sum is homogeneous over the segment. However, the largest cumulative displacement occurring during
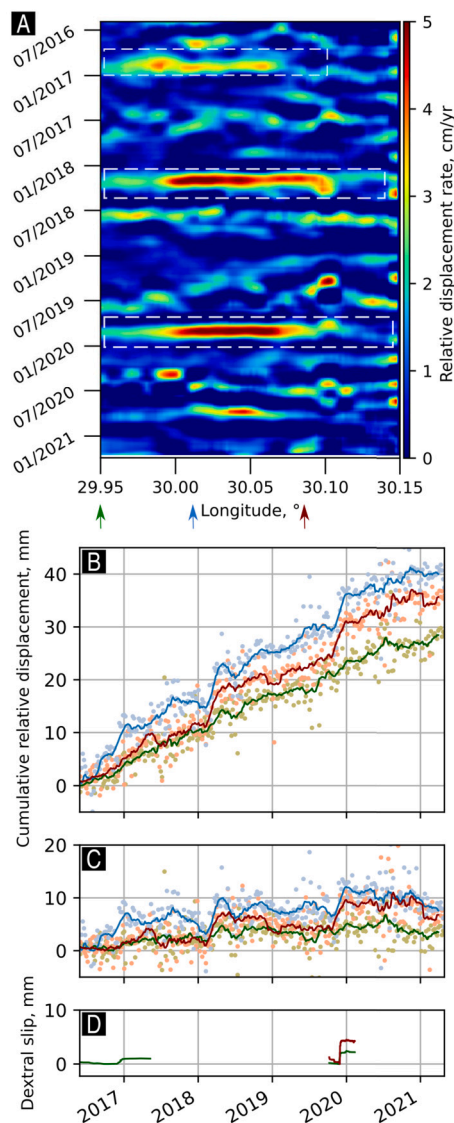
Fig. 3. Spatial and temporal evolution of the East-West relative displacements along the Izmit segment. (A) East-West relative displacement rate along the Izmit segment estimated by using a 50 *days* average sliding window, using pixels from 400 *m* to 1000 *m* away from the fault. The pixels used are shown in Fig. S11. Three high amplitude periods are delimited by white dotted rectangles, corresponding to an increase of relative displacement rates above 4 *cm/yr*. The arrows below the figure correspond to the location of the profiles shown on panels (B) and (C), green and red corresponding to the locations of the Izmit and Tepetarla creepmeters, respectively. (B) Cumulative East-West relative displacement estimated at three longitudes, by using pixels from 600 *m*-width boxes. The lines correspond to the 60 *days* average sliding windows. (C) Corresponding detrended cumulative East-West relative displacement time series obtained after the removal of the linear trend between the transient accelerations. (D) Creepmeter records over the analyzed period of time, green and red corresponding to Izmit and Tepetarla creepmeters, respectively.

the transient periods is located on the central part of the segment, with a difference of at least 10 *mm* of total displacement between the middle and the edges of the segment. The proportion of displacements due to both periods varies along the segment. On the middle of the segment, 50% of the cumulative deformation is due to the transient events, against only 25 − 30% at the edges. Note that these ratios depend on the distance from the fault trace chosen to compute the relative displacements. For example, the creepmeters located right on the fault capture only the transient events and no relative displacements before or after

the events (Fig. 3D), suggesting that only the slip during the transient events reach the surface while the inter-transient slip might be deeper.

5.2. Slip inference at depth

In this section, we estimate the slip distribution along the Izmit segment of the NAF from surface InSAR East-West displacement time series. We perform independent inversions for the static displacement during transient SSEs and for the linear velocity associated with steady creep estimated in between transient events. The inverse models formalism is explained in the Appendix E.

5.2.1. Steady-state creep

To study the linear trend observed on the time series between transient SSEs, we adjust the time series segments by removing the transient SSE offsets and compute the mean velocity using a linear regression (Fig. 5A). The fault-perpendicular profile shown on the Fig. 5B is focused closer to the fault than the profile shown Fig. 2E and enables to confirm the relative long-term velocity of the NAF (McClusky et al., 2000; Reilinger et al., 2006; Nocquet, 2012).

We perform a series of inversions to constrain the locking depth in the deep part of the fault, using as inversion parameters 1500 *m* for λ_0, 2500 *m* for λ and 0.5 for σ_m, parameters selected by computing the slip roughness as a function of the RMS and selecting the values with the L-curve criterion (Hansen, 1992) (Fig. S19A). We conduct several inversions with varying locking depths in the *a priori* model m_0 ranging from 0 to 30 *km*, with slip rate below the locking depth fixed to the relative plate motion of 24 *mm/yr* (McClusky et al., 2000; Reilinger et al., 2006; Nocquet, 2012). We compute the RMS errors as a function of the *a priori* locking depths (Fig. S16) and investigate the slip models (Fig. S17). For *a priori* locking depths below 10 *km*, the RMS are large and the slip models cannot explain the displacement away from the fault (Fig. S18), because of too shallow locking depths together with the slip positivity constraint preventing to obtain smaller slip amplitudes fitting the data. For locking depths below 15 *km*, deep patches with unrealistic slip amplitudes are appearing in the slip models to counterbalance too deep locking depths. We thus estimate the optimal locking depth at 11 *km*, to both fit the data and obtain an homogeneous slip distribution below the locking depth. The corresponding slip distribution is presented in the Fig. 6A (the deeper part is shown on Fig. S17B), and shows homogeneous slip below the locking depth as well as shallow creep. The residuals between the preferred model prediction and the observations are shown in Fig. S18H.

The final slip distribution (Fig. 6A) shows shallow slip, mostly from 2 to 4 *km*, with slip rates of 2 *cm/yr* and up to 6 *cm/yr* at the longitude $E029.99°$. This shallow slip is located right below the sedimentary basin as constrained by gravity measurements (Özalaybey et al., 2011). Other slip patches closer to the surface are located to the east of the Izmit segment, below the Sapanca Lake, at longitude $E030.18°$. The lateral roughness of shallow creep is poorly constrained by the data, which prevents us to study the along-strike slip rate variations. Several models obtained with distinct spatial smoothing in slip rate equally explain the observations (examples Fig. S20). However, the depth distribution is well constrained, independently of the spatial smoothing, with high slip rates between 2 and 4 *km* depth.

5.2.2. Transient slow slip events

After the removal of the linear inter-transient velocity studied previously (Fig. 5A), we compute the total displacement during each SSE by averaging the displacements 1 *month* before and after the transient periods and computing the difference, at each pixel. The three maps on the Fig. 5 - C, D and E are the total East-West displacement fields obtained for the 2016, 2018, and 2019 events, respectively. The locations of the three fault-perpendicular profiles (Fig. 5 - F, G and H) have been selected at the maximum relative displacements along the fault for each transient event. The three profiles show a strong gradient with different
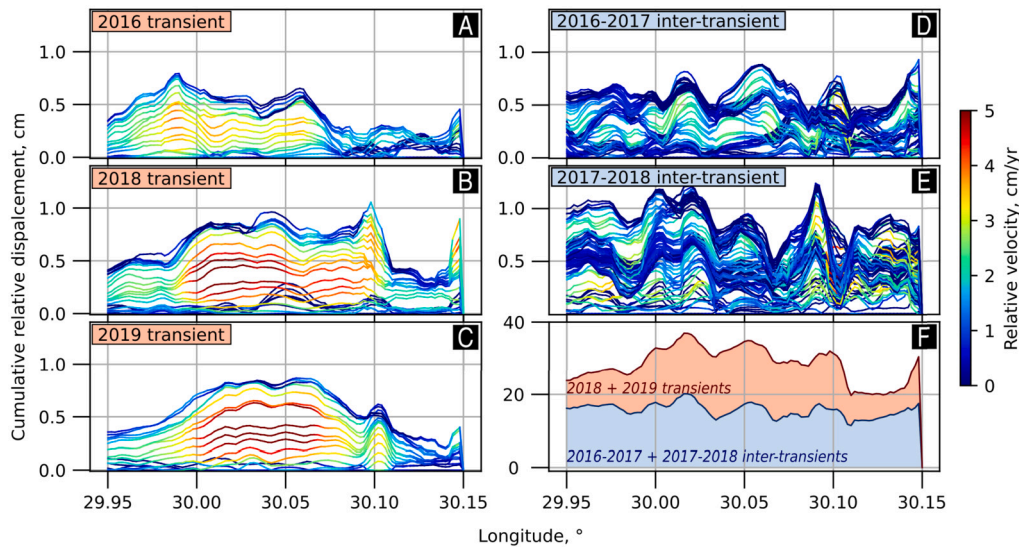
Fig. 4. Relative cumulative displacement recorded during (A, B, C) and in between (D, E) three transient events highlighted by the white dotted rectangles in the Fig. 3A: in December 2016, in March 2018 and in November 2019. Two inter-transient periods are therefore defined, between the 2016 (from October 10, 2016 to January 20, 2017) and 2018 (from January 1st, 2018 to May 20, 2018) events and 2018 and 2019 (from October 10, 2019 to January 10, 2020) events. (F) Sum of the relative cumulative displacement during the transient (red) and inter-transient (blue) periods. The pixels used to build this figure are shown in Fig. S11. Similar results obtained with the pair of tracks *TA160-D138* are shown in Fig. S12.
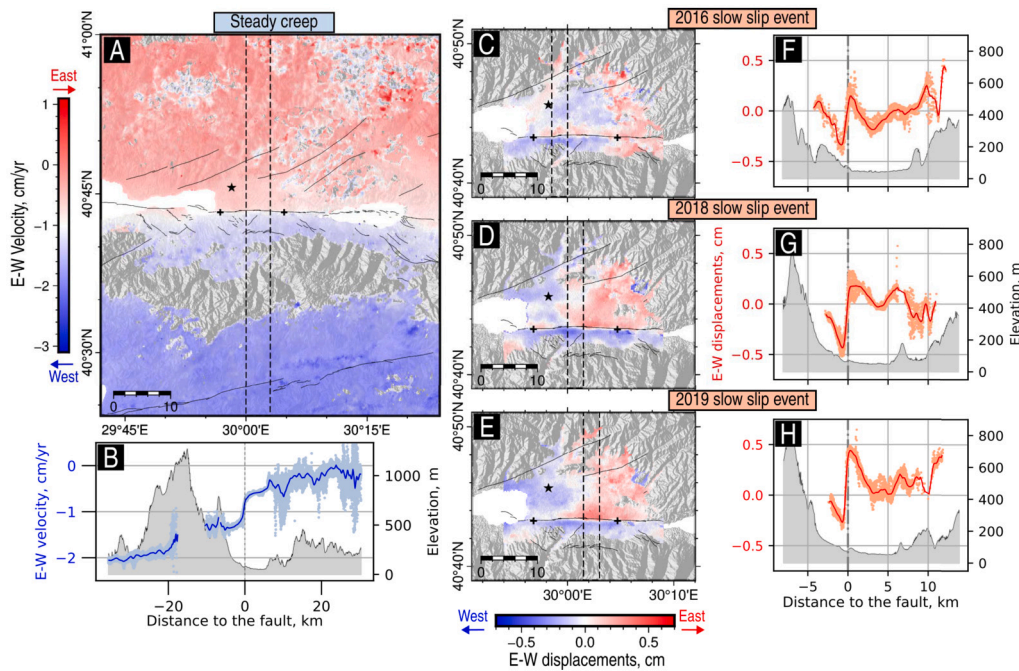

Fig. 5. East-West velocity field during the continuous creep periods and East-West static offsets during the transient slow slip events. (A) Surface velocity computed during the steady-state creep periods. (B) Fault-perpendicular profile (location on A with the dashed lines) of the East-West velocity and of the mean elevation. (C-E) Static displacements offsets estimated during the three transient slow slip events in 2016 (C), 2018 (D) and 2019 (E). (F-H) Associated fault-perpendicular profiles from each map. The corresponding results obtained with the pair of tracks *TA160-D138* are shown in Fig. S13.

amplitudes: $\sim 5\ mm$, $\sim 8\ mm$ and $\sim 9\ mm$ for the 2016, 2018 and 2019 events, respectively. While the signal associated with the 2016 event appears more noisy on the map, the 2018 and 2019 events are characterized by positive and negative lobes on each side of the fault.

We conduct inversions to estimate the slip at depth associated with the 2018 and 2019 SSEs. Taking into account the strong gradients of the East-West displacement fields observed across the fault, we choose to consider only the part of the interface below the Izmit segment from the surface to 5 km. The Fig. 6 - B and C shows the results of the inverse model computation for the 2018 and 2019 transient events, respec-

tively, using as inversion parameters $m_0 = 0$, $\lambda_0 = 333\ m$, $\lambda = 2500\ m$ (2018 event) and $\lambda = 2000\ m$ (2019 event) and $\sigma_m = 0.5$. λ is selected based on the L-curve criterion (Fig. S19B and S19C). Different models with varying λ are shown in Figs. S22 and S23. RMS errors obtained when comparing the preferred model predictions to the data are shown in Fig. S21. The main slipping patches are concentrated on the upper part of the fault interface, above 2 km-depth, within or close to the downdip limit of the sedimentary basin. In both slip distributions, the slip is mostly localized on the central part of the Izmit segment, with a mean East-West displacement of about $\sim 3\ cm$. We observe two main
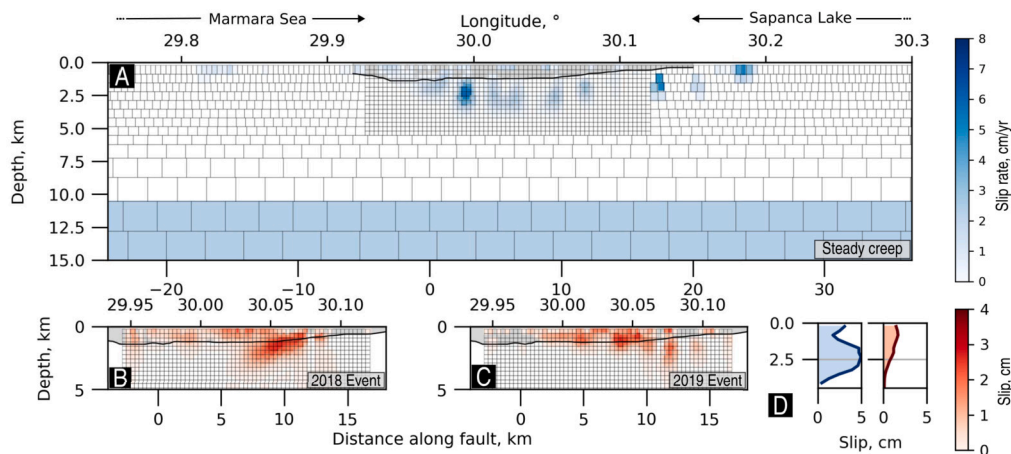
Fig. 6. Fault slip models for the steady creep and the 2018 and 2019 slow slip events. (A) Preferred slip model obtained for the steady creep, with an *a priori* locking depth at 11 *km*-depth. (B-C) Slip models obtained for the 2018 and 2019 slow slip events. The gray area underlined by a black thick line corresponds to the sedimentary basin obtained from gravity data by Özalaybey et al. (2011). The distance along fault is computed from the 1999 Izmit earthquake epicenter. (D) Depth distribution of the cumulative slip during the two complete cycles of transient and inter-transient periods (from the October 10, 2016 to January 10, 2020). The blue and red parts correspond to the creep during the inter-transient and transient periods, respectively. It has been computed within the tightened mesh, below the Izmit segment.

slipping areas, a smaller one on the western part ($\sim 3\ km^2$) and a bigger one on the central part of the interface with a size about $\sim 8\ km^2$. Both are located within or just slightly below the sedimentary basin. It suggests that the same slipping areas ruptured by both SSEs. By using a mean shear modulus of 18 GPa for the first 4 km of the fault interface and slipping areas of 11.4 and 9.3 km^2 for the 2018 and 2019 transient events, respectively, we obtain equivalent magnitudes of 4.4 and 4.3 (Hanks and Kanamori, 1979). Thus, the predicted North-South displacements related to each slip distribution reveal amplitudes lower than 0.1 mm, validating the assumption of a negligible North-South displacement along the Izmit segment.

6. Discussion

The InSAR data used in this study results from the automatic processing made in the framework of the FLATSIM project briefly described in section 3.1. We applied specific post-processing including referencing, denoising and sources decomposition (section 3) allowing us to extract a tectonic signal related to the spatio-temporal evolution of the slip on the Izmit segment of the NAF (section 5). Our results confirm that the products of this automatic processing are suitable not only for the analysis of continental deformation (Lemrabet et al., 2023), but also for the analysis of a regional (within a 200 km^2 region) and slow (a few mm for the transient events) deformation. Our post-processing analysis enables to correct the InSAR data from seasonal signals, as well as (i) large-scale signals included in the whole tracks, extracted using a trajectory model approach (section 4.3) and (ii) local signals located within the Izmit sedimentary basin and extracted using ICA (section 3.5). These seasonal signals (Figs. S4, S9 and S10) can be related to several mechanisms not studied here (e.g. hydrological or atmospheric residuals effects), and their spatial analysis reveal that no clear tectonic signal was contained in both types of signal, meaning that the creep along the Izmit segment is not seasonally modulated.

6.1. Steady creep along the Izmit segment

Our results confirm that the Izmit segment is still aseismically creeping 22 *years* after the 1999 Izmit earthquake. To compare the cumulative displacements along the segment before and after the Izmit earthquake, we use two survey GNSS stations SISL and SMAS located 3 km away from the fault (black dots in Fig. 1C) combined with published InSAR time series (Cakir et al., 2012; Hussain et al., 2016) as well as InSAR

time series from this study. The Fig. S24 shows the East-West component of the SMAS-SISL baseline computed for the 1995-2019 period after removing the interseismic linear trend before the earthquake (Özarpacı et al., 2020). We used the logarithmic decay with a relaxation time of 60 yr provided by Özarpacı et al. (2020) based on the SMAS-SISL baseline to model the postseismic phase. As mentioned by Özarpacı et al. (2020), this logarithmic evolution suggests that the postseismic phase is still on-going. The InSAR time series from this study, with $\sim 5\ mm/yr$ of baseline increase rate during the period 2015-2021, fit well with the logarithmic decay.

The shallow steady-state creep estimated in this study, occurs within the shallowest 5 km of the fault (Fig. 7). Coseismic models of the 1999 Izmit earthquake (Delouis et al., 2002; Feigl et al., 2002) suggest that $2-3\ m$ of slip occurs in the first 5 km while the slip reached a maximum value of 7 m around 6 to 8 km-depth. This is leading to 4 to 5 m of slip deficit in the shallow section of the fault. Postseismic slip estimates are discontinuous in time in the published literature. Early postseismic models suggest that $5-9\ cm$ of slip occurred on the first 5 km of the Izmit segment during the first 10 $days$ (Bürgmann et al., 2002; Ergintav et al., 2002). However, we have no constraints on the amplitude of early afterslip that occurred within the first few hours after the earthquake, which could reach up to 10% of the coseismic slip amplitude (Twardzik et al., 2019). Later estimates of the postseismic creep rate on the first kilometers of the fault ($\leq 5\ km$-depth) are coming from InSAR studies: $\sim 10\ mm/yr$ from 2002 to 2010 (Cakir et al., 2012; Ergintav et al., 2014; Hussain et al., 2016), $\sim 8\ mm/yr$ from 2011 to 2017 (Aslan et al., 2019; Özarpacı et al., 2020) and $\sim 7.5\ mm/yr$ from 2016 to 2021 estimated by our study. Taking into account all these estimates plus the observation that 2/3 of the relaxation occurred within the first two years based on the logarithmic decay for the baseline between GNSS sites SISL and SMAS (Fig. S24), we obtain a rough estimate of a cumulative shallow postseismic slip of $\sim 35\ cm$, representing less than 10% of the coseismic slip deficit, in agreement with the analysis from Özarpacı et al. (2020). Such a small amount of shallow postseismic slip with large uncertainties could mean that either a large part of the early shallow afterslip is missing in the published models or that the coseismic deficit was overestimated (e.g. due to neglected off-fault yielding) or that postseismic afterslip can still last for several decades to catch-up the deficit, like on the NAF Ismetpasa segment still creeping at the surface about eighty years after the 1944 M_w7.3 Bolu-Gerede earthquake (Jolivet et al., 2023).
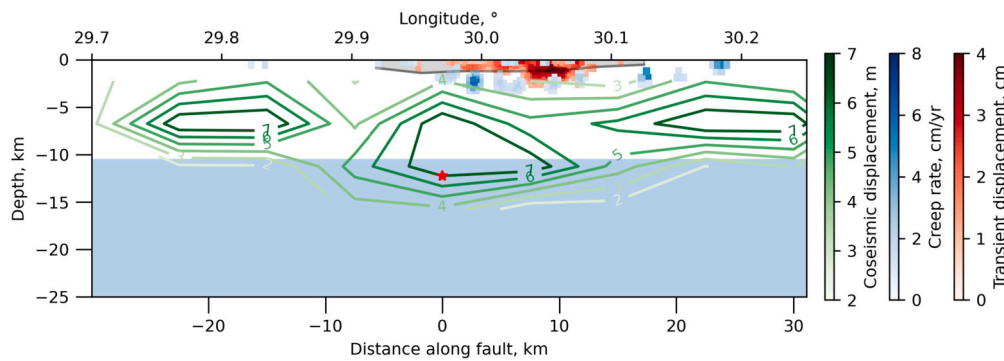
Fig. 7. 2D fault interface of the Izmit segment with the slip distributions at distinct phases of the seismic cycle. The green lines delimit the coseismic slip distribution from Delouis et al. (2002). The blue colorbar corresponds to the steady creep with homogeneous creep at 24 mm/yr below 11 km depth and steady creep patches between 2 and 4 km depth. The red colorbar corresponds to the sum of both slip distributions obtained by inversions of the total displacements during the 2018 and the 2019 slow slip events. The gray area corresponds to the bottom of the sedimentary basin obtained from gravity data by Özalaybey et al. (2011). The red star corresponds to the 1999 Izmit earthquake hypocenter. The distance along fault is computed from the 1999 Izmit earthquake epicenter.

Our inverse models with varying *a priori* locking depths (section 5.2.1), suggest an optimal locking depth of ∼ 11 km along the Izmit segment during the 2016-2021 period. Reilinger et al. (2006) found a locking depth of 21 km before the 1999 earthquake, whereas studies for the periods after the earthquake found locking depths from 10 to 12 km (Cakir et al., 2012; Aslan et al., 2019; Özarpacı et al., 2020), in agreement with our result, except for Hussain et al. (2016) who found a deeper locking depth of ∼ 18 km. The shallow locking depth in the two decades after the Izmit earthquake together with the deeper one estimated before the earthquake is favoring a still active postseismic afterslip below the seismogenic zone, with deepening of the locking depth throughout the seismic cycle. A shallow locking depth is also observed along the Ismetpasa segment of the NAF by Jolivet et al. (2023), who found locking depths of about 8 − 12 km below the creeping segment and 15 − 20 km below the locked surrounding segments. As proposed by Jolivet et al. (2023), the shallow locking depth below some segments may potentially be a key factor in terms of stress transfers for the establishment of long-lasting continuous shallow creep during the interseismic phase.

6.2. Izmit slow slip event cycle

Up to now, four SSEs have been detected along the Izmit segment: in September 2015 (Özarpacı et al., 2020), in December 2016 (this study and Aslan et al., 2019), in March 2018 and in November 2019 (this study), corresponding to an averaged return period of ∼ 1.3 *years*. Such a recurrence interval is on the same order of magnitude to the ones observed on the California faults segments with shallow SSEs, including the Superstition Hills Fault or the San Andreas Fault near San Juan Bautista (Wei et al., 2013). The recurrence intervals of SSEs on the Ismetpasa creeping section of the NAF was also of ∼ 1 *yr* in the 80's and between 2014 and 2016 (Bilham et al., 2016). This recurrence interval might increase in the future if the Izmit segment is still in its postseismic phase or can stay steady if the fault is already back in its interseismic phase (Wei et al., 2013). In between SSEs, we observe steady-state creep that is localized below. When looking at the slip rate variations during these periods of time, they are not steady in time (Fig. 4 - D and E) and might suggest the presence of lower amplitude transient slip events. However, these variations are at the noise level, preventing us to identify smaller amplitude SSEs. All scenarios between end-members continuous slip and successions of small amplitude SSEs are possible for the slip dynamics between 2 and 4 km-depth.

Among the four SSEs of the Izmit segment observed so far, only the 2018 and 2019 events have a signal complete enough to get estimates of associated slip at depth. The 2015 event has been observed only with the Izmit creepmeter recording 1.6 mm of dextral displacement (Aslan et al., 2019). The 2016 event has been observed both with the Izmit
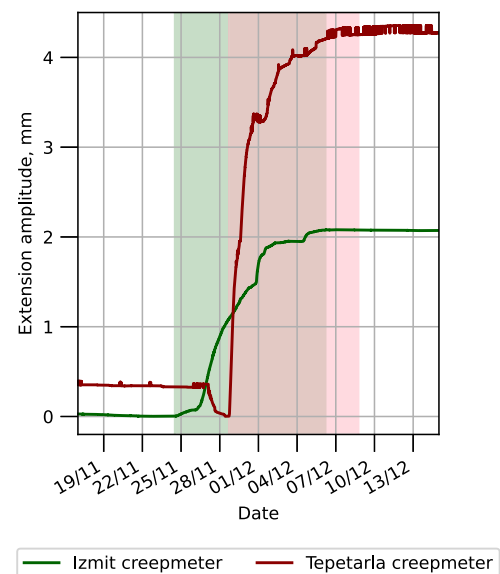

Fig. 8. Creepmeter records from Izmit (in green) and Tepetarla (in red) during the 2019 event. The lines correspond to the raw records and the rectangles correspond to the transient event periods.

creepmeter recording 1.1 mm of dextral displacement and 10 mm of InSAR East-West relative displacement by Aslan et al. (2019) and 5 mm of East-West InSAR relative displacement in our analysis. The maximum relative displacement (Fig. 4A) is located on the western part of the Izmit segment. Slip amplitudes for both 2018 and 2019 SSEs are around 1 to 2 cm and can reach up to 6 cm depending on spatial smoothing. The slip is mainly located on the central part of the Izmit segment for both of these events, suggesting a potential migration compared to the 2016 event. The associated equivalent moment magnitudes for these two events are 4.4 and 4.3. The slip characteristics in terms of depth, shape of the slipping asperity and amplitudes are equivalent to other models of shallow SSEs on the Ismetpasa segment of the NAF (Rousset et al., 2016) or on the Superstition Hills Fault (Wei et al., 2009). These SSEs on the Izmit segment allow the release of 48 − 51% of the plate loading velocity, when computing the loading moment rate on the same area than the one used to compute the equivalent moment of the events.

To estimate the durations of the transient events, we analyzed the creepmeters records, the 6 *days* InSAR temporal sampling being too sparse to estimate precisely the durations of the SSEs. Fig. 8 shows the records of both creepmeters for the 2019 event, with a sampling of 30 *sec*. The start of the event is obvious with a sharp onset. We esti-

mate the end of an event as the time for which the pre-transient trend is being recovered. For the Izmit creepmeter (Fig. 8 in green), the event started on November 26, 2019 at 10am GMT and ended on December 6, 2019 at 9am GMT, corresponding to a total duration of 9 *days* and 23 *hours*. For the Tepetarla record (Fig. 8 in red), the event started on November 28, 2019 at 5pm GMT and ended the December 7, 2019 at 1pm GMT, corresponding to a total duration of 8 *days* and 21 *hours*.

By using the total duration of about 9 *days* and the equivalent moment magnitude of 4.3 for the 2019 event estimated from the slip models, we can compare these characteristics with other worldwide SSEs. These values are in agreement with shallow continental strike slip faults SSEs on the Ismetasa segment of the NAF (Rousset et al., 2016), on the Superstition Hills Fault (Wei et al., 2009) and the Imperial Fault (Materna et al., 2024). Compared to subduction SSEs, these events have lower moment magnitudes, but the duration that can be equivalent to some short-term subduction events. In a moment magnitude versus duration plot, they fall to the left of the linear relation between duration and moment magnitude obtained by gathering all subduction SSEs and tremors (Materna et al., 2024). As suggested by Ide and Beroza (2023), these events take place within the hidden area due to the lack of observational results for small magnitude events in subduction zones.

The onset of the 2019 SSE is shifted by 2.26 *days* between both creepmeters. By using the distance of ~ 14.5 *km* between them, and assuming a unilateral rupture with constant velocity, we estimate a propagation velocity from Izmit to Tepetarla of ~ 6.4 *km/day*, comparable with the ones observed for propagating events on the San Andreas Fault (Gittins and Hawthorne, 2022; Materna et al., 2024). It is also comparable with the along-strike propagation velocities of subduction SSEs in Nankai (Obara and Sekine, 2009), Cascadia (Bartlow et al., 2011) and Alaska (Rousset et al., 2019). Given that there is only two observation points to estimate the onset of the 2019 Izmit SSE, it is also possible that this event propagated bi-laterally, starting in between the two creepmeters and would lead to a propagation velocity between 0 and 6.4 *km/day* depending on the initiation location.

6.3. Possible mechanisms promoting creep and SSEs along the Izmit segment

Our analysis of the slip rate on the Izmit segment reveals two distinct slip modes: steady creep between 2 and 4 *km* and transient SSEs between the surface and 2 *km* depth (Fig. 7). The presence of shallow aseismic slip within the first 4 *km* is likely due to a compensation of slip deficit from the 1999 Izmit earthquake coseismic slip at seismogenic depths. Both slip modes observed at shallow depth are possibly due to depth variations of frictional properties, the shallow SSEs being located within or close to the downdip limit of a sedimentary basin. The continuous creep between 2 and 4 *km* might be a necessary condition to drive the shallow SSEs by continuously increasing the shear stress on the first kilometers of the fault.

In the framework of rate-and-state friction models, the depth-dependence of the frictional parameters explains the various seismic and aseismic slip modes for strike-slip faults. An unstable velocity-weakening layer at seismogenic depth overlaying a velocity-strengthening layer at deeper depths explains cycles of large earthquakes (e.g. Lapusta et al., 2000; Barbot et al., 2012). The addition of a velocity-strengthening zone within the first kilometers of the fault can explain shallow aseismic creep (Kaneko et al., 2013). By adding even more complexities to the frictional variations within the first kilometers of the faults, including variations between conditionally stable velocity-neutral and velocity-strengthening layers, Wei et al. (2013) and Tymofyeyeva et al. (2019) show that the emergence of shallow transient aseismic slip events is possible. In the particular case of the Izmit segment, two key features have to be explained, (i) a logarithmic decay associated to the postseismic afterslip as observed by the pair of GNSS sites SISL and SMAS (Fig. S24) and (ii) the emergence of transient slip events. The models derived by Wei et al. (2013) including a small con-

ditionally stable layer close to the surface succeed to explain both of these observations. This model predicts a shortening of the recurrence SSE intervals within the postseismic phase. However, we cannot estimate such an evolution with the limited number of events observed so far on the Izmit segment.

The distribution between creeping segments (e.g. Ismetpasa and Izmit) and locked segments along the NAF remains unclear, although a mineralogical control is often evoked. Within the Izmit area, the northern branch of the NAF splits two bedrocks units composed of (i) limestones from the Paleozoic-Mesozoic sequence on the northern side and (ii) several metamorphic units on the southern side, both deposited on a metamorphic basement (Akbayram et al., 2013; Kaduri et al., 2017; Taylor et al., 2019). The mineralogical analysis of the gouge of the Ismetpasa creeping segment from Kaduri et al. (2017) suggests that the volcanic units are more prone to be affected by both seismic and aseismic slip than the limestone ones. In the case of the Izmit segment, the contrast between the northern and the southern units is in agreement with geological conditions which can promote aseismic creep according to Kaduri et al. (2017). The shallow sediments are usually clay-rich (e.g. Rockwell et al., 2009), which can also promote the development of creep (Bürgmann, 2018). In addition, a tomography study from Taylor et al. (2019) shows that the damaged zone within the crust goes down to 5 *km* below the Izmit segment surface trace, compatible with the depth of the creeping zone.

High pore fluid pressure can also enhance the presence of transient aseismic slip as evidenced by tomography with high Vp/Vs ratio at subduction zones areas prone to SSEs (Shelly et al., 2006). In geothermal contexts, aseismic slip seems also to be the favored mechanisms to release the accumulated stress on local faults (e.g. Guglielmi et al., 2015). On strike-slip faults, intense rain events have been suggested to favor transient creep events (Roeloffs, 2001). Seasonal modulation of creep has been observed on some faults, like the SAF (Li et al., 2023), which could be due to seasonal variations of either pore pressure or regional hydrological surface loading. On the Izmit segment of the NAF, we analyzed the seasonal components of the time series (section 4.3) and found no clear evidence of seasonal modulation of creep. To evidence any potential correlation with meteorological events, we looked at temperature and precipitation data from the ERA-5 Land data during the 2016-2021 period (Fig. S25). We do not see clear relationship between temperature variations, cumulative precipitations and the transient event occurrences. However, the 2016 transient event coincides with a period of increased precipitations, which could potentially have an effect on pore pressure of the fault interface. The topographical low of the Izmit basin together with the sedimentary basin may also favor an overall high pore pressure within the basin.

Finally, we looked at the AFAD earthquake catalog over the 2016-2021 period to detect any link between seismicity within the Izmit basin and the SSEs (Fig. S26). The temporal distribution of the events seems to be random over the 5 *years*-long period, and no obvious link between these events and the SSEs can be inferred. The location of the events (Fig. S26A) reveals a seismically quiescent area corresponding to the central part of the Izmit segment, where the SSEs slip amplitude is the highest (Fig. 4F), suggesting a spatial segmentation between seismicity and transient aseismic SSEs. We also looked for possible triggering by regional large earthquakes and found no events at the times of the shallow SSEs, suggesting that they are spontaneous SSEs.

7. Conclusions

By employing automated InSAR time series analysis and subsequent processing, we investigated the slip dynamics of the Izmit segment of the North Anatolian Fault from 2016 to 2021. Our results reveal a locked zone at 11 *km* depth and aseismic creep within the upper 5 *km*, likely compensating for the 1999 Izmit earthquake's slip deficit. The temporal analysis of the creep combined with slip inverse models show that steady creep is occurring $2-4$ *km*-depth while transient slow slip events

are happening from the surface to 2 km-depth. The depth separation between these two slip modes is likely due to frictional variations, the SSEs being located at the downdip limit of the sedimentary basin and above it. We detected two new SSEs, leading to four SSEs observed along this segment since the 1999 Izmit earthquake: in September 2015, December 2016, March 2018 and November 2019; corresponding to an average return period of 1.3 $years$. The slip models of the 2018 and 2019 events correspond to equivalent moment magnitudes of 4.4 and 4.3, respectively. The creepmeter recordings at two sites allow to extract a propagation velocity of 6.4 km/day for the 2019 event. The presence of a transient slow slip event cycle 22 $years$ after the Izmit earthquake might last for decades when comparing to the Ismetpasa segment of the NAF where slow slip events are still happening 80 years after the 1944 Gerede-Bolu earthquake.

CRediT authorship contribution statement

Estelle Neyrinck: Writing – original draft, Methodology, Investigation. **Baptiste Rousset:** Writing – review & editing, Supervision, Methodology, Conceptualization. **Cécile Doubre:** Writing – review & editing, Supervision, Methodology, Conceptualization. **Luis Rivera:** Writing – review & editing, Methodology. **Cécile Lasserre:** Writing – review & editing, Validation, Data curation. **Marie-Pierre Doin:** Validation, Data curation. **Philippe Durand:** Data curation. **Roger Bilham:** Data curation. **Ziyadin Çakir:** Data curation. **FLATSIM Working Group:** Data curation.

Declaration of competing interest

The authors declare that they have no known competing financial interests or personal relationships that could have appeared to influence the work reported in this paper.

Appendix A. Method of InSAR referencing relative to GNSS velocities

We project the GNSS velocities into the LOS components for each track, only using the horizontal eastward and northward GNSS components. We then extract the mean InSAR LOS velocities within a 1 km-diameter circle surrounding each GNSS station to compare them with the GNSS velocities. We compute a 2D plane corresponding to the difference between the estimated mean InSAR LOS velocities and the GNSS velocities. By subtracting the 2D plane to our InSAR velocities, we obtain a LOS velocity field relative to fixed Eurasia.

Appendix B. Seasonal signals extraction

We model the seasonal signal using a linear and annual periodic terms:

$$x(t) = x_R + B.(t - t_0) + C.sin(2\pi(t - t_0)) + D.cos(2\pi(t - t_0)) \quad \text{(B.1)}$$

with $x(t)$ the cumulative LOS displacement at each pixel at time t, t_0 the initial time (here January 1st, 2015) and x_R a constant term. B represents the linear trend of the signal. C and D correspond to the seasonal amplitudes with periods of one year (cosine and sine correspond to the summer/winter and spring/autumn cycles for a t_0 on January 1st, respectively). The best parameters are estimated independently for each pixel of each track in a least-square sense. The seasonal amplitudes (C and D components) are locally referenced by subtracting a 4th order fitting surface in order to not be dependent on the signal amplitude of the unwrapping reference point.

Appendix C. Horizontal/vertical decomposition

We interpolate the LOS time series to be on the same spatial and temporal basis for the three tracks, by building a new spatial grid using a 0.001°-side square mesh (the initial grids having a 8 $looks$ resolution corresponding to a 120 m pixel size (Thollard et al., 2021)) and interpolating each time series with it. Then, we define a new time vector with 6 $days$-intervals, minimizing the time between the initial acquisition times of the three tracks and the interpolated one, coinciding with the days of acquisitions of the tracks A058 and D138, acquired the same day but with an interval of 12 $hours$ (D1308 is acquired at 4am and A058 is acquired at 4pm). The time interpolation is linear. Since Sentinel-1 acquisitions shifted from 12 $days$ revisit times before April 25, 2016 to 6 $days$-intervals afterward, we only use data acquired after May 1st, 2016, for consistency.

We then use the following equations to project the LOS ascending and descending displacements onto the fault-parallel (horizontal) and vertical directions (e.g. Fialko et al., 2002):

$$P = \begin{pmatrix} e_{asc}sin\alpha + n_{asc}cos\alpha & u_{asc} \\ e_{dec}sin\alpha + n_{dec}cos\alpha & u_{dec} \end{pmatrix} \quad \text{(C.1)}$$

$$\begin{pmatrix} x_{f,t} \\ x_{z,t} \end{pmatrix} = P^{-1} \begin{pmatrix} x_{asc,t} \\ x_{dec,t} \end{pmatrix} \quad \text{(C.2)}$$

with P a rotation matrix, α the mean strike of the fault (in this case 90°), (e_i, n_i, u_i) the Cartesian components of the satellite look vectors for the ascending and the descending tracks (noted asc and dec, respectively), $x_{i,t}$ the LOS displacement, and $(x_{f,t}, x_{z,t})$ the component of the displacement along the fault-parallel direction and the vertical direction, respectively, at time t.

Appendix D. Independent component analysis (ICA)

Independent Component Analysis (ICA) assumes that a signal X can be represented as a mixture of several independent sources S so that $X = A * S$, where A is a mixture matrix. The sources are estimated in order to estimate sources as independent as possible (Hyvärinen and Oja, 2000). We use the *FastICA* algorithm from the *scikit-learn* Python library.

We determine the optimal number of IC components by comparing the InSAR time series variances with the variance of the reconstructed time series using a variable number of IC components (Fig. S3). Three components enable to explain almost 80% of the InSAR data variance (shown in Fig. S4), including one component exhibiting a temporal linear trend (figure S4E). In order not to get rid of potential tectonic signal, we only remove the two components without temporal linear trends (Fig. S4 - D and F). By checking differential time series between two pixels on opposite sides of the fault, we verify that the tectonic signal is unaffected by the removal of the noise components (e.g. Fig. S5).

Appendix E. Inverse models formalism

To estimate the depth and amplitude of slip on the fault interface, we invert the InSAR surface displacement or velocity field by using the generalized least square solution (Tarantola and Valette, 1982):

$$m = m_0 + (G^t.C_d^{-1}.G + C_m^{-1})^{-1}.G^t.C_d^{-1}.(d - G.m_0) \quad \text{(E.1)}$$

where m is the strike-slip distribution on the fault plane, m_0 the *a priori* model (non-zero only for the steady creep inversions), G the Green's functions relating unit slip on a given fault patch to the surface displacement field, C_d the data covariance matrix, C_m the model covariance matrix and d the InSAR data. We add a positivity constraint on m of positive right-lateral strike-slip motion by using the non-negative least square algorithm (Lawson and Hanson, 1995). We compute covariograms for each dataset to estimate the spatial covariance C (Sudhaus and Jónsson, 2009):

$$C(h_C) = \frac{1}{2N} \sum_{i=1}^{N} (d(r_i).d(s_i)) \quad \text{(E.2)}$$

where r_i and s_i are two pixels, $h_C = ||r_i - s_i||$ is the distance between both pixels, N is the total number of pairs and d the observed displacements per pixel. The matrix C_d is made of the spatial covariance C for each pixel within the study zone. We compute a covariance matrix, using the following equation (e.g. Radiguet et al., 2011):

$$C_m = \left(\sigma_m.\frac{\lambda_0}{\lambda}\right)^2 e^{-\frac{a}{\lambda}} \quad \text{(E.3)}$$

with σ_m the standard deviation of the model parameters, λ_0 a scaling factor, λ the correlation distance, and a the distance between fault patches.

To compute the Green's functions G, we consider a multi-layered elastic half-space (Zhu and Rivera, 2002). The velocity model (Karabulut, 2024) as well as the density model for the sedimentary basin (Özalaybey et al., 2011) and for the deeper part (Crust 1.0, Laske et al., 2013)) are shown in Fig. S14. This layered structure is important for the study area to take into account the low velocities and low densities within the Izmit basin, and avoid estimation bias of the shallow slip. The fault is meshed with tight patches of 333 m by 333 m below the Izmit segment down to 5 km. The mesh is coarser around and down to 35 km with patches size increasing from 750 m by 1000 m meters at the surface to 5000 m by 5000 m at depth. For the steady creep estimation between transient SSEs, we estimate tectonic loading from the side by computing Green's functions for 4060 km-long and 35 km-deep fault patches. Below, we use a soft medium with near zero velocities. Such a medium has no resistance against the above-imposed fault motion and thus move together with both plates. A comparison with an infinite fault in an elastic medium shows that this boundary condition produces equivalent deformation amplitudes in the far field at a much reduced computational cost (Fig. S15). The scaling factor λ_0 being determined using the mean distance between the patches, we use 1500 m for the continuous creep using the whole mesh and 333 m for the transient creep events inversions using only the tightened mesh.

Appendix F. Supplementary material

Supplementary material related to this article can be found online at https://doi.org/10.1016/j.epsl.2024.119104.

Data availability

The authors do not have permission to share data.

References

Akbayram, K., Okay, A.I., Satır, M., 2013. Early Cretaceous closure of the Intra-Pontide Ocean in western Pontides (northwestern Turkey). J. Geodyn. 65, 38–55. https://doi.org/10.1016/j.jog.2012.05.003. https://www.sciencedirect.com/science/article/pii/S0264370712000877.

Aslan, G., Lasserre, C., Cakir, Z., Ergintav, S., Özarpaci, S., Dogan, U., Bilham, R., Renard, F., 2019. Shallow creep along the 1999 Izmit earthquake rupture (Turkey) from GPS and high temporal resolution interferometric synthetic aperture radar data (2011–2017). J. Geophys. Res., Solid Earth 124, 2218–2236. https://doi.org/10.1029/2018JB017022. https://onlinelibrary.wiley.com/doi/abs/10.1029/2018JB017022.

Avouac, J.P., 2015. From geodetic imaging of seismic and aseismic fault slip to dynamic modeling of the seismic cycle. Annu. Rev. Earth Planet. Sci. 43, 233–271. https://doi.org/10.1146/annurev-earth-060614-105302.

Barbot, S., Lapusta, N., Avouac, J.P., 2012. Under the hood of the earthquake machine: toward predictive modeling of the seismic cycle. Science 336, 707–710.

Barka, A., 2002. The surface rupture and slip distribution of the 17 August 1999 Izmit earthquake (M 7.4), North Anatolian fault. Bull. Seismol. Soc. Am. 92, 43–60. https://doi.org/10.1785/0120000841. https://pubs.geoscienceworld.org/bssa/article/92/1/43-60/102910.

Bartlow, N.M., Miyazaki, S., Bradley, A.M., Segall, P., 2011. Space-time correlation of slip and tremor during the 2009 Cascadia slow slip event. Geophys. Res. Lett. 38. https://doi.org/10.1029/2011GL048714. https://onlinelibrary.wiley.com/doi/abs/10.1029/2011GL048714. https://onlinelibrary.wiley.com/doi/pdf/10.1029/2011GL048714.

Bilham, R., Ozener, H., Mencin, D., Dogru, A., Ergintav, S., Cakir, Z., Aytun, A., Aktug, B., Yilmaz, O., Johnson, W., Mattioli, G., 2016. Surface creep on the North Anatolian fault at Ismetpasa, Turkey, 1944-2016: North Anatolian fault creep. J. Geophys. Res., Solid Earth 121, 7409–7431. https://doi.org/10.1002/2016JB013394. http://doi.wiley.com/10.1002/2016JB013394.

Bouchon, M., Bouin, M.P., Karabulut, H., Toksöz, M.N., Dietrich, M., Rosakis, A.J., 2001. How fast is rupture during an earthquake? New insights from the 1999 Turkey earthquakes. Geophys. Res. Lett. 28, 2723–2726. https://doi.org/10.1029/2001GL013112. https://onlinelibrary.wiley.com/doi/abs/10.1029/2001GL013112. https://onlinelibrary.wiley.com/doi/pdf/10.1029/2001GL013112.

Bürgmann, R., 2018. The geophysics, geology and mechanics of slow fault slip. Earth Planet. Sci. Lett. 495, 112–134. https://doi.org/10.1016/j.epsl.2018.04.062. https://linkinghub.elsevier.com/retrieve/pii/S0012821X18302760.

Bürgmann, R., Ergintav, S., Segall, P., Hearn, E.H., McClusky, S., Reilinger, R.E., Woith, H., Zschau, J., 2002. Time-dependent distributed afterslip on and deep below the Izmit earthquake rupture. Bull. Seismol. Soc. Am. 92, 126–137.

Çakir, Z., Chabalier, J.B.d., Armijo, R., Meyer, B., Barka, A., Peltzer, G., 2003. Coseismic and early post-seismic slip associated with the 1999 Izmit earthquake (Turkey), from SAR interferometry and tectonic field observations. Geophys. J. Int. 155, 93–110. https://doi.org/10.1046/j.1365-246X.2003.02001.x. https://academic.oup.com/gji/article-lookup/doi/10.1046/j.1365-246X.2003.02001.x.

Cakir, Z., Ergintav, S., Ozener, H., Dogan, U., Akoglu, A.M., Meghraoui, M., Reilinger, R., 2012. Onset of aseismic creep on major strike-slip faults. Geology 40, 1115–1118. https://doi.org/10.1130/G33522.1. https://pubs.geoscienceworld.org/geology/article/40/12/1115-1118/130811.

Delouis, B., Giardini, D., Lundgren, P., Salichon, J., 2002. Joint inversion of insar, gps, teleseismic, and strong-motion data for the spatial and temporal distribution of earthquake slip: application to the 1999 Izmit mainshock. Bull. Seismol. Soc. Am. 92, 278–299.

Doin, M.P., Lodge, F., Guillaso, S., Jolivet, R., Lasserre, C., Ducret, G., Grandin, R., Pathier, E., Pinel, V., 2011. Presentation of the small baseline NSBAS processing chain on a case example: the Etna deformation monitoring from 2003 to 2010 using ENVISAT data, 8.

Dragert, H., Wang, K., James, T.S., 2001. A silent slip event on the deeper Cascadia subduction interface. Science 292, 1525–1528. https://doi.org/10.1126/science.1060152. https://www.science.org/doi/10.1126/science.1060152.

Emre, Ö., Duman, T.Y., Özalp, S., Şaroğlu, F., Olgun, C., Elmacı, H., Çan, T., 2018. Active fault database of Turkey. Bull. Earthq. Eng. 16, 3229–3275. https://doi.org/10.1007/s10518-016-0041-2.

England, P., Houseman, G., Nocquet, J.M., 2016. Constraints from GPS measurements on the dynamics of deformation in Anatolia and the Aegean. J. Geophys. Res., Solid Earth 121, 8888–8916. https://doi.org/10.1002/2016JB013382. https://onlinelibrary.wiley.com/doi/abs/10.1002/2016JB013382. https://onlinelibrary.wiley.com/doi/pdf/10.1002/2016JB013382.

Ergintav, S., Bürgmann, R., McClusky, S., Çakmak, R., Reilinger, R.E., Lenk, O., Barka, A., Özener, H., 2002. Postseismic deformation near the İzmit earthquake (17 August 1999, M 7.5) rupture zone. Bull. Seismol. Soc. Am. 92, 194–207. https://doi.org/10.1785/0120000836.

Ergintav, S., McClusky, S., Hearn, E., Reilinger, R., Cakmak, R., Herring, T., Ozener, H., Lenk, O., Tari, E., 2009. Seven years of postseismic deformation following the 1999, M = 7.4 and M = 7.2, Izmit-Düzce, Turkey earthquake sequence. J. Geophys. Res., Solid Earth 114. https://doi.org/10.1029/2008JB006021. https://onlinelibrary.wiley.com/doi/abs/10.1029/2008JB006021. https://onlinelibrary.wiley.com/doi/pdf/10.1029/2008JB006021.

Ergintav, S., Reilinger, R.E., Çakmak, R., Floyd, M., Cakir, Z., Doğan, U., King, R.W., McClusky, S., Özener, H., 2014. Istanbul's earthquake hot spots: geodetic constraints on strain accumulation along faults in the Marmara seismic gap. Geophys. Res. Lett. 41, 5783–5788. https://doi.org/10.1002/2014GL060985. https://onlinelibrary.wiley.com/doi/abs/10.1002/2014GL060985. https://onlinelibrary.wiley.com/doi/pdf/10.1002/2014GL060985.

Feigl, K.L., Sarti, F., Vadon, H., McClusky, S., Ergintav, S., Durand, P., Bürgmann, R., Rigo, A., Massonnet, D., Reilinger, R., 2002. Estimating slip distribution for the Izmit mainshock from coseismic gps, ers-1, radarsat, and spot measurements. Bull. Seismol. Soc. Am. 92, 138–160.

Fialko, Y., Sandwell, D., Agnew, D., Simons, M., Shearer, P., Minster, B., 2002. Deformation on nearby faults induced by the 1999 Hector Mine earthquake.

Science 297, 1858–1862. https://doi.org/10.1126/science.1074671. https://www.science.org/doi/10.1126/science.1074671.

Gittins, D.B., Hawthorne, J.C., 2022. Are creep events big? Estimations of along-strike rupture lengths. J. Geophys. Res., Solid Earth 127, e2021JB023001. https://doi.org/10.1029/2021JB023001. https://onlinelibrary.wiley.com/doi/abs/10.1029/2021JB023001. https://onlinelibrary.wiley.com/doi/pdf/10.1029/2021JB023001.

Grandin, R., 2015. Interferometric processing of SLC Sentinel-1 TOPS data. In: FRINGE'15: Advances in the Science and Applications of SAR Interferometry and Sentinel-1 InSAR Workshop. Frascati, Italy, 23-27 March 2015, Frascati, Italy. https://hal.science/hal-01621519.

Guglielmi, Y., Cappa, F., Avouac, J.P., Henry, P., Elsworth, D., 2015. Seismicity triggered by fluid injection–induced aseismic slip. Science 348, 1224–1226. https://doi.org/10.1126/science.aab0476. https://www.science.org/doi/full/10.1126/science.aab0476.

Hanks, T.C., Kanamori, H., 1979. A moment magnitude scale. J. Geophys. Res., Solid Earth 84, 2348–2350. https://doi.org/10.1029/JB084iB05p02348. https://agupubs.onlinelibrary.wiley.com/doi/10.1029/JB084iB05p02348.

Hansen, P.C., 1992. Analysis of discrete ill-posed problems by means of the L-curve. SIAM Rev. 34, 561–580. https://doi.org/10.1137/1034115. https://epubs.siam.org/doi/abs/10.1137/1034115.

Hearn, E.H., Bürgmann, R., Reilinger, R.E., 2002. Dynamics of İzmit earthquake postseismic deformation and loading of the Düzce earthquake hypocenter. Bull. Seismol. Soc. Am. 92, 172–193. https://doi.org/10.1785/0120000832.

Hearn, E.H., McClusky, S., Ergintav, S., Reilinger, R.E., 2009. Izmit earthquake postseismic deformation and dynamics of the North Anatolian fault zone. J. Geophys. Res., Solid Earth 114. https://doi.org/10.1029/2008JB006026. https://onlinelibrary.wiley.com/doi/abs/10.1029/2008JB006026. https://onlinelibrary.wiley.com/doi/pdf/10.1029/2008JB006026.

Hussain, E., Wright, T.J., Walters, R.J., Bekaert, D., Hooper, A., Houseman, G.A., 2016. Geodetic observations of postseismic creep in the decade after the 1999 Izmit earthquake, Turkey: implications for a shallow slip deficit: IZMIT CREEP. J. Geophys. Res., Solid Earth 121, 2980–3001. https://doi.org/10.1002/2015JB012737. http://doi.wiley.com/10.1002/2015JB012737.

Hyvärinen, A., Oja, E., 2000. Independent component analysis: algorithms and applications. Neural Netw. 13, 411–430.

Ide, S., Beroza, G.C., 2023. Slow earthquake scaling reconsidered as a boundary between distinct modes of rupture propagation. Proc. Natl. Acad. Sci. 120, e2222102120. https://doi.org/10.1073/pnas.2222102120. https://www.pnas.org/doi/abs/10.1073/pnas.2222102120.

Inbal, A., Ampuero, J.P., Avouac, J.P., 2017. Locally and remotely triggered aseismic slip on the central San Jacinto fault near Anza, CA, from joint inversion of seismicity and strainmeter data. J. Geophys. Res., Solid Earth 122, 3033–3061. https://doi.org/10.1002/2016JB013499. https://onlinelibrary.wiley.com/doi/abs/10.1002/2016JB013499. https://onlinelibrary.wiley.com/doi/pdf/10.1002/2016JB013499.

Jiang, Y., Wdowinski, S., Dixon, T.H., Hackl, M., Protti, M., Gonzalez, V., 2012. Slow slip events in Costa Rica detected by continuous GPS observations, 2002–2011. Geochem. Geophys. Geosyst. 13. https://doi.org/10.1029/2012GC004058. https://onlinelibrary.wiley.com/doi/abs/10.1029/2012GC004058. https://onlinelibrary.wiley.com/doi/pdf/10.1029/2012GC004058.

Jolivet, R., 2011. Déformation intersismique le long de la faille de Haiyuan, Chine: variations spatio-temporelles contraintes par interférométrie SAR. PhD Thesis. Université de Grenoble.

Jolivet, R., Lasserre, C., Doin, M.P., Guillaso, S., Peltzer, G., Dailu, R., Sun, J., Shen, Z.K., Xu, X., 2012. Shallow creep on the haiyuan fault (Gansu, China) revealed by sar interferometry. J. Geophys. Res., Solid Earth 117.

Jolivet, R., Jara, J., Dalaison, M., Rouet-Leduc, B., Özdemir, A., Dogan, U., Çakir, Z., Ergintav, S., Dubernet, P., 2023. Daily to centennial behavior of aseismic slip along the central section of the North Anatolian fault. J. Geophys. Res., Solid Earth 128, e2022JB026018. https://doi.org/10.1029/2022JB026018. https://onlinelibrary.wiley.com/doi/abs/10.1029/2022JB026018. https://onlinelibrary.wiley.com/doi/pdf/10.1029/2022JB026018.

Kaduri, M., Gratier, J.P., Renard, F., Çakir, Z., Lasserre, C., 2017. The implications of fault zone transformation on aseismic creep: example of the North Anatolian fault, Turkey. J. Geophys. Res., Solid Earth 122, 4208–4236. https://doi.org/10.1002/2016JB013803. https://onlinelibrary.wiley.com/doi/abs/10.1002/2016JB013803. https://onlinelibrary.wiley.com/doi/pdf/10.1002/2016JB013803.

Kaneko, Y., Fialko, Y., Sandwell, D.T., Tong, X., Furuya, M., 2013. Interseismic deformation and creep along the central section of the North Anatolian fault (Turkey): InSAR observations and implications for rate-and-state friction properties. J. Geophys. Res., Solid Earth 118, 316–331. https://doi.org/10.1029/2012JB009661. https://onlinelibrary.wiley.com/doi/abs/10.1029/2012JB009661. https://onlinelibrary.wiley.com/doi/pdf/10.1029/2012JB009661.

Karabulut, H., 2024. High resolution p-wave tomography of the rupture zone of 1999 Izmit and Duzce earthquake. Geophys. J. Int. Submitted for publication.

Karabulut, H., Schmittbuhl, J., Özalaybey, S., Lengliné, O., Kömeç-Mutlu, A., Durand, V., Bouchon, M., Daniel, G., Bouin, M., 2011. Evolution of the seismicity in the eastern Marmara sea a decade before and after the 17 August 1999 Izmit earthquake. Tectonophysics 510, 17–27. https://doi.org/10.1016/j.tecto.2011.07.009. https://linkinghub.elsevier.com/retrieve/pii/S0040195111002903.

Klein, E., Duputel, Z., Masson, F., Yavasoglu, H., Agram, P., 2017. Aseismic slip and seismogenic coupling in the Marmara sea: what can we learn from on-land geodesy? Geophys. Res. Lett. 44, 3100–3108. https://doi.org/10.1002/2017GL072777. https://onlinelibrary.wiley.com/doi/abs/10.1002/2017GL072777. https://onlinelibrary.wiley.com/doi/pdf/10.1002/2017GL072777.

LaBonte, A.L., Brown, K.M., Fialko, Y., 2009. Hydrologic detection and finite element modeling of a slow slip event in the Costa Rica prism toe. J. Geophys. Res., Solid Earth 114.

Lapusta, N., Rice, J.R., Ben-Zion, Y., Zheng, G., 2000. Elastodynamic analysis for slow tectonic loading with spontaneous rupture episodes on faults with rate- and state-dependent friction. J. Geophys. Res., Solid Earth 105, 23765–23789. https://doi.org/10.1029/2000JB900250. https://onlinelibrary.wiley.com/doi/abs/10.1029/2000JB900250. https://onlinelibrary.wiley.com/doi/pdf/10.1029/2000JB900250.

Laske, G., Masters, G., Ma, Z., Pasyanos, M., 2013. Update on CRUST1.0 - a 1-degree Global Model of Earth's Crust.

Lawson, C.L., Hanson, R.J., 1995. Solving Least Squares Problems. SIAM. Google-Books-ID: AEwDbHp50FgC.

Lemrabet, L., Doin, M.p., Lasserre, C., Durand, P., 2023. Referencing of continental-scale insar-derived velocity fields: case study of the eastern Tibetan Plateau. J. Geophys. Res., Solid Earth 128, e2022JB026251.

Li, Y., Bürgmann, R., Taira, T., 2023. Spatiotemporal variations of surface deformation, shallow creep rate, and slip partitioning between the San Andreas and southern Calaveras fault. J. Geophys. Res., Solid Earth 128, e2022JB025363. https://doi.org/10.1029/2022JB025363. https://onlinelibrary.wiley.com/doi/abs/10.1029/2022JB025363. https://onlinelibrary.wiley.com/doi/pdf/10.1029/2022JB025363.

Materna, K., Bürgmann, R., Lindsay, D., Bilham, R., Herring, T., Crowell, B., Szeliga, W., 2024. Shallow slow slip events in the imperial valley with along-strike propagation. Geophys. Res. Lett. 51, e2023GL108089. https://doi.org/10.1029/2023GL108089. https://onlinelibrary.wiley.com/doi/abs/10.1029/2023GL108089. https://onlinelibrary.wiley.com/doi/pdf/10.1029/2023GL108089.

Maubant, L., Pathier, E., Daout, S., Radiguet, M., Doin, M.P., Kazachkina, E., Kostoglodov, V., Cotte, N., Walpersdorf, A., 2020. Independent component analysis and parametric approach for source separation in InSAR time series at regional scale: application to the 2017–2018 slow slip event in Guerrero (Mexico). J. Geophys. Res., Solid Earth 125, e2019JB018187. https://doi.org/10.1029/2019JB018187. https://onlinelibrary.wiley.com/doi/abs/10.1029/2019JB018187. https://onlinelibrary.wiley.com/doi/pdf/10.1029/2019JB018187.

McCaffrey, R., Wallace, L.M., Beavan, J., 2008. Slow slip and frictional transition at low temperature at the hikurangi subduction zone. Nat. Geosci. 1, 316–320.

McClusky, S., Balassanian, S., Barka, A., Demir, C., Ergintav, S., Georgiev, I., Gurkan, O., Hamburger, M., Hurst, K., Kahle, H., Kastens, K., Kekelidze, G., King, R., Kotzev, V., Lenk, O., Mahmoud, S., Mishin, A., Nadariya, M., Ouzounis, A., Paradissis, D., Peter, Y., Prilepin, M., Reilinger, R., Sanli, I., Seeger, H., Tealeb, A., Toksöz, M.N., Veis, G., 2000. Global positioning system constraints on plate kinematics and dynamics in the eastern Mediterranean and Caucasus. J. Geophys. Res., Solid Earth 105, 5695–5719. https://doi.org/10.1029/1999JB900351. https://onlinelibrary.wiley.com/doi/abs/10.1029/1999JB900351. https://onlinelibrary.wiley.com/doi/pdf/10.1029/1999JB900351.

Nocquet, J.M., 2012. Present-day kinematics of the Mediterranean: a comprehensive overview of GPS results. Tectonophysics 579, 220–242. https://doi.org/10.1016/j.tecto.2012.03.037. https://www.sciencedirect.com/science/article/pii/S0040195112001953.

Obara, K., Sekine, S., 2009. Characteristic activity and migration of episodic tremor and slow-slip events in central Japan. Earth Planets Space 61, 853–862. https://doi.org/10.1186/BF03353196.

Obara, K., Hirose, H., Yamamizu, F., Kasahara, K., 2004. Episodic slow slip events accompanied by non-volcanic tremors in southwest Japan subduction zone. Geophys. Res. Lett. 31. https://doi.org/10.1029/2004GL020848. https://onlinelibrary.wiley.com/doi/abs/10.1029/2004GL020848. https://onlinelibrary.wiley.com/doi/pdf/10.1029/2004GL020848.

Özalaybey, S., Zor, E., Ergintav, S., Tapırdamaz, M.C., 2011. Investigation of 3-D basin structures in the İzmit Bay area (Turkey) by single-station microtremor and gravimetric methods. Geophys. J. Int. 186, 883–894. https://doi.org/10.1111/j.1365-246X.2011.05085.x.

Özarpacı, S., Doğan, U., Ergintav, S., Çakır, Z., Özdemir, A., Floyd, M., Reilinger, R., 2020. Present GPS velocity field along 1999 Izmit rupture zone: evidence for continuing afterslip 20 yr after the earthquake. Geophys. J. Int. 224, 2016–2027. https://doi.org/10.1093/gji/ggaa560. https://academic.oup.com/gji/article/224/3/2016/5992340.

Radiguet, M., Cotton, F., Vergnolle, M., Campillo, M., Valette, B., Kostoglodov, V., Cotte, N., 2011. Spatial and temporal evolution of a long term slow slip event: the 2006 Guerrero slow slip event. Geophys. J. Int. 184, 816–828. https://doi.org/10.1111/j.1365-246X.2010.04866.x.

Reilinger, R., McClusky, S., Vernant, P., Lawrence, S., Ergintav, S., Cakmak, R., Ozener, H., Kadirov, F., Guliev, I., Stepanyan, R., Nadariya, M., Hahubia, G., Mahmoud, S., Sakr, K., ArRajehi, A., Paradissis, D., Al-Aydrus, A., Prilepin, M., Guseva, T., Evren, E., Dmitrotsa, A., Filikov, S.V., Gomez, F., Al-Ghazzi, R., Karam, G., 2006. GPS constraints on continental deformation in the Africa-Arabia-Eurasia continental collision zone and implications for the dynamics of plate interactions. J. Geophys. Res., Solid Earth 111. https://doi.org/10.1029/2005JB004051. https://onlinelibrary.wiley.

com/doi/abs/10.1029/2005JB004051. https://onlinelibrary.wiley.com/doi/pdf/10.1029/2005JB004051.

Rockwell, T., Ragona, D., Seitz, G., Langridge, R., Aksoy, M.E., Ucarkus, G., Ferry, M., Meltzner, A.J., Klinger, Y., Meghraoui, M., Satir, D., Barka, A., Akbalik, B., 2009. Palaeoseismology of the North Anatolian Fault near the Marmara Sea: implications for fault segmentation and seismic hazard. Geol. Soc. (Lond.) Spec. Publ. 316, 31–54. https://doi.org/10.1144/SP316.3. https://www.lyellcollection.org/doi/10.1144/SP316.3.

Roeloffs, E.A., 2001. Creep rate changes at Parkfield, California 1966–1999: seasonal, precipitation induced, and tectonic. J. Geophys. Res., Solid Earth 106, 16525–16547. https://doi.org/10.1029/2001JB000352. https://onlinelibrary.wiley.com/doi/abs/10.1029/2001JB000352. https://onlinelibrary.wiley.com/doi/pdf/10.1029/2001JB000352.

Rousset, B., Jolivet, R., Simons, M., Lasserre, C., Riel, B., Mililio, P., Çakir, Z., Renard, F., 2016. An aseismic slip transient on the North Anatolian fault. Geophys. Res. Lett. 43, 3254–3262. https://doi.org/10.1002/2016GL068250. https://onlinelibrary.wiley.com/doi/10.1002/2016GL068250.

Rousset, B., Fu, Y., Bartlow, N., Bürgmann, R., 2019. Weeks-long and years-long slow slip and tectonic tremor episodes on the south central Alaska megathrust. J. Geophys. Res., Solid Earth 124, 13392–13403. https://doi.org/10.1029/2019JB018724. https://onlinelibrary.wiley.com/doi/abs/10.1029/2019JB018724. https://onlinelibrary.wiley.com/doi/pdf/10.1029/2019JB018724.

Scholz, C.H., 1998. Earthquakes and friction laws. Nature 391, 37–42. https://doi.org/10.1038/34097. https://www.nature.com/articles/34097.

Shelly, D.R., Beroza, G.C., Ide, S., Nakamula, S., 2006. Low-frequency earthquakes in Shikoku, Japan, and their relationship to episodic tremor and slip. Nature 442, 188–191. https://doi.org/10.1038/nature04931. https://www.nature.com/articles/nature04931.

Stein, R.S., Barka, A.A., Dieterich, J.H., 1997. Progressive failure on the North Anatolian fault since 1939 by earthquake stress triggering. Geophys. J. Int. 128, 594–604. https://doi.org/10.1111/j.1365-246X.1997.tb05321.x. https://academic.oup.com/gji/article-lookup/doi/10.1111/j.1365-246X.1997.tb05321.x.

Steinbrugge, K.V., Zacher, E.G., Tocher, D., Whitten, C.A., Claire, C.N., 1960. Creep on the San Andreas fault. Bull. Seismol. Soc. Am. 50, 389–415. https://doi.org/10.1785/BSSA0500030389.

Sudhaus, H., Jónsson, S., 2009. Improved source modelling through combined use of InSAR and GPS under consideration of correlated data errors: application to the June 2000 Kleifarvatn earthquake, Iceland. Geophys. J. Int. 176, 389–404. https://doi.org/10.1111/j.1365-246X.2008.03989.x. https://academic.oup.com/gji/article-lookup/doi/10.1111/j.1365-246X.2008.03989.x.

Tarantola, A., Valette, B., 1982. Generalized nonlinear inverse problems solved using the least squares criterion. Rev. Geophys. 20, 219. https://doi.org/10.1029/RG020i002p00219. http://doi.wiley.com/10.1029/RG020i002p00219.

Taylor, G., Rost, S., Houseman, G.A., Hillers, G., 2019. Near-surface structure of the North Anatolian fault zone from Rayleigh and Love wave tomography using ambient seismic noise. Solid Earth 10, 363–378. https://doi.org/10.5194/se-10-363-2019. https://se.copernicus.org/articles/10/363/2019/.

Thollard, F., Clesse, D., Doin, M.P., Donadieu, J., Durand, P., Grandin, R., Lasserre, C., Laurent, C., Deschamps-Ostanciaux, E., Pathier, E., Pointal, E., Proy, C., Specht, B., 2021. FLATSIM: the ForM@Ter LArge-scale multi-temporal Sentinel-1 InterferoMetry service. Remote Sens. 13, 3734. https://doi.org/10.3390/rs13183734. https://www.mdpi.com/2072-4292/13/18/3734.

Twardzik, C., Vergnolle, M., Sladen, A., Avallone, A., 2019. Unravelling the contribution of early postseismic deformation using sub-daily GNSS positioning. Sci. Rep. 9, 1775. https://doi.org/10.1038/s41598-019-39038-z. https://www.nature.com/articles/s41598-019-39038-z.

Tymofyeyeva, E., Fialko, Y., Jiang, J., Xu, X., Sandwell, D., Bilham, R., Rockwell, T.K., Blanton, C., Burkett, F., Gontz, A., Moafipoor, S., 2019. Slow slip event on the southern San Andreas fault triggered by the 2017 M8.2 Chiapas (Mexico) earthquake. J. Geophys. Res., Solid Earth 124, 9956–9975. https://doi.org/10.1029/2018JB016765. https://onlinelibrary.wiley.com/doi/10.1029/2018JB016765.

Vaca, S., Vallée, M., Nocquet, J.M., Battaglia, J., Régnier, M., 2018. Recurrent slow slip events as a barrier to the northward rupture propagation of the 2016 Pedernales earthquake (central Ecuador). Tectonophysics 724–725, 80–92. https://doi.org/10.1016/j.tecto.2017.12.012. https://www.sciencedirect.com/science/article/pii/S0040195117305152.

Vavra, E.J., Fialko, Y., Rockwell, T., Bilham, R., Štěpančíková, P., Stemberk, J., Tábořík, P., Stemberk, J., 2024. Characteristic slow-slip events on the superstition hills fault, southern California. Geophys. Res. Lett. 51, e2023GL107244.

Wallace, L.M., Webb, S.C., Ito, Y., Mochizuki, K., Hino, R., Henrys, S., Schwartz, S.Y., Sheehan, A.F., 2016. Slow slip near the trench at the Hikurangi subduction zone, New Zealand. Science 352, 701–704. https://doi.org/10.1126/science.aaf2349. https://www.science.org/doi/full/10.1126/science.aaf2349.

Wang, L., Wang, R., Roth, F., Enescu, B., Hainzl, S., Ergintav, S., 2009. Afterslip and viscoelastic relaxation following the 1999 M 7.4 İzmit earthquake from GPS measurements. Geophys. J. Int. 178, 1220–1237. https://doi.org/10.1111/j.1365-246X.2009.04228.x.

Wei, M., Sandwell, D., Fialko, Y., 2009. A silent M 4.7 slip event of October 2006 on the Superstition Hills fault, southern California. J. Geophys. Res., Solid Earth 114. https://doi.org/10.1029/2008JB006135. https://onlinelibrary.wiley.com/doi/abs/10.1029/2008JB006135. https://onlinelibrary.wiley.com/doi/pdf/10.1029/2008JB006135.

Wei, M., Sandwell, D., Fialko, Y., Bilham, R., 2011. Slip on faults in the Imperial Valley triggered by the 4 April 2010 Mw 7.2 El Mayor-Cucapah earthquake revealed by InSAR. Geophys. Res. Lett. 38. https://doi.org/10.1029/2010GL045235. https://onlinelibrary.wiley.com/doi/abs/10.1029/2010GL045235. https://onlinelibrary.wiley.com/doi/pdf/10.1029/2010GL045235.

Wei, M., Kaneko, Y., Liu, Y., McGuire, J., 2013. Episodic fault creep events in California controlled by shallow frictional heterogeneity. Nat. Geosci. 6, 566–570. https://doi.org/10.1038/ngeo1835.

Zhu, L., Rivera, L.A., 2002. A note on the dynamic and static displacements from a point source in multilayered media. Geophys. J. Int. 148, 619–627. https://doi.org/10.1046/j.1365-246X.2002.01610.x.